

Article

Evolution of Structure and Texture Formation in Thermomechanically Treated Ti-Zr-Nb Shape Memory Alloys

Alexandra Baranova¹, Sergey Dubinskiy^{1,*}, Irina Vvedenskaya¹, Andrey Bazlov², Natalia Tabachkova^{3,4}, Vadim Sheremetyev¹, Tatyana Teplyakova^{1,5}, Oleg Strakhov¹ and Sergey Prokoshkin¹

- ¹ Laboratory of Shape Memory Alloys, National University of Science and Technology MISIS, Leninskiy Prospect. 4, p. 1., 119049 Moscow, Russia; baranova.al.pavlovna@yandex.ru (A.B.); vvkarak@yandex.ru (I.V.); sheremetyev@misis.ru (V.S.); t.teplyakova95@mail.ru (T.T.); strakhovo2018@gmail.com (O.S.); sprokoshkin@mail.ru (S.P.)
- ² Department of Physical Metallurgy of Non Ferrous Metals, National University of Science and Technology MISIS, Leninskiy Prospect. 4, p. 1., 119049 Moscow, Russia; bazlov@misis.ru
- ³ Department of Materials Science of Semiconductors and Dielectrics, National University of Science and Technology MISIS, Leninskiy Prospect. 4, p. 1., 119049 Moscow, Russia; ntabachkova@gmail.com
- ⁴ Department of Nanotechnology, Prokhorov General Physics Institute of the Russian Academy of Sciences, 38 Vavilov Str., 119991 Moscow, Russia
- ⁵ Laboratory of Electronography, National Research Center Kurchatov Institute, Academician Kurchatov Square, 1, 123182 Moscow, Russia
- * Correspondence: dubinskiy.sm@misis.ru; Tel.: +7-916-8470-539

Abstract: Biomedical Ti-22Nb-6Zr, Ti-18Zr-15Nb, and Ti-41Zr-12Nb (at.%) shape memory alloys were subjected to cold rolling (CR) and subsequent post-deformation annealing (PDA). The evolutions of phase and structure states, crystallographic texture, and crystallographic limit of recovery strain were studied using EBSD, TEM, and XRD analyses. The study found that CR ($e = 1.5$) and PDA at 800 °C for 30 min results in fine- and coarse-grained structures. Severe CR ($e = 3.0$) and PDA at 550 °C for 5 min results in a recrystallized, equiaxed, predominantly ultrafine-grained structure of the β -phase with a small amount of low-angle boundaries. Increasing the degree of CR from moderate ($e = 0.3$) to severe ($e = 3.0$) results in a favorable strong $\{111\}_{\beta} <110>_{\beta}$ recrystallization texture. Alloys with low Zr content are more susceptible to this type of crystallographic texture formation during TMT, primarily due to a higher Nb content. The Ti-41Zr-12Nb alloy shows the highest crystallographic limit of recovery strain ($\epsilon_r^{max} \approx 6\%$). The limit decreases to $\approx 5\%$ (for Ti-18Zr-15Nb) and $\approx 3\%$ (for Ti-22Nb-6Zr) when transitioning from high- to low-Zr alloys. The transition of Ti-Zr-Nb alloys from coarse-grained to ultrafine-grained structures of the β -phase and a decrease in grain size do not affect the crystallographic limit of recovery strain in the studied grain size ranges.

Keywords: Ti-Zr-Nb shape memory alloys; thermomechanical treatment; phase state; microstructure; X-ray diffraction (XRD); EBSD; TEM; crystallographic limit of recovery strain



Citation: Baranova, A.; Dubinskiy, S.; Vvedenskaya, I.; Bazlov, A.; Tabachkova, N.; Sheremetyev, V.; Teplyakova, T.; Strakhov, O.; Prokoshkin, S. Evolution of Structure and Texture Formation in Thermomechanically Treated Ti-Zr-Nb Shape Memory Alloys. *Appl. Sci.* **2024**, *14*, 3647. <https://doi.org/10.3390/app14093647>

Academic Editors: Vineet V. Joshi, David Field and Rajib Kalsar

Received: 27 March 2024

Revised: 18 April 2024

Accepted: 20 April 2024

Published: 25 April 2024



Copyright: © 2024 by the authors. Licensee MDPI, Basel, Switzerland. This article is an open access article distributed under the terms and conditions of the Creative Commons Attribution (CC BY) license (<https://creativecommons.org/licenses/by/4.0/>).

1. Introduction

Ti-Zr-Nb shape memory alloys (SMAs), initially niobium- and lately zirconium-enriched, are promising materials for bone implants [1–9]. This is primarily due to their high biomechanical and biochemical compatibilities. Their biomechanical compatibility is a result of their relatively low Young's modulus (≤ 50 GPa) and non-linear superelastic mechanical behavior, which is similar to that of bone tissue [1–3,10–14]. Their biochemical compatibility is due to the presence of only biocompatible elements in their composition [15–17]. The basic purpose of constructing Ti-Zr-Nb SMAs is to identify their superelastic behavior at operating temperature, i.e., human body temperature, as a result of reversible stress-induced $\beta \leftrightarrow \alpha''$ martensitic transformation [2,7,18,19]. Previous studies have shown that zirconium as an alloying element in combination with niobium is quite effective for increasing the crystallographic limit of recovery strain (ϵ_r^{max}) [19]. Thus, the

amount of Zr is optimized to achieve superelastic behavior at human body temperature. Historically, all Ti-Zr-Nb SMAs have been classified into three groups: (1) low-Zr alloys (Ti-22Nb-6Zr, for example); (2) medium-Zr alloys (Ti-18Zr-15Nb), and (3) high-Zr alloys (Ti-41Zr-12Nb) (all in at.%).

Low-Zr alloys: The Ti-22Nb-6Zr shape memory alloy is an evolution of the binary Ti-22Nb SMA [2,20]. Besides increasing the crystallographic limit of recovery strain and realizing superelastic behavior at human body temperature, the addition of zirconium helps to control ω -phase precipitation upon cooling in the course of heat treatment [21,22]. However, this alloy has a relatively low crystallographic limit of recovery strain of about 3%, which limits the maximum superelastic strain and functional fatigue resistance.

Medium-Zr alloys: The Ti-18Zr-(14–15)Nb SMA is a highly developed and promising second-generation Zr-rich alloy [15,23,24]. This alloy has a higher crystallographic limit of recovery strain of about 5.5% due to its higher zirconium and lower niobium content, which positively affects the maximum superelastic strain and number of cycles to failure during functional cycling tests [24,25].

High-Zr alloys: Further Zr enrichment and transition to Ti-(40–44)Zr-(10–12)Nb are expected to increase the crystallographic limit of recovery strain to 7–8% [19,23,26]. These alloys hold promise for the third generation of Ti-Zr-Nb-based SMAs.

All functional properties of Ti-based SMAs are structure-sensitive. Therefore, to obtain optimal functional properties, it is necessary to optimize the structural/phase state and crystallographic texture of the alloy [25,27–29]. Grain and/or subgrain refinement, down to submicrometer and nanometer sizes, drastically increases the dislocation yield stress, which in turn increases the difference between the dislocation and transformation yield stresses. This leads to an improved realization of recovery strain or recovery stress and enhances superelasticity and shape memory effect characteristics [30,31]. Furthermore, shape recovery properties are also sensitive to the crystal lattice orientation. The maximum recovery strain in β -titanium SMAs can be achieved in the $\{001\}_\beta \langle 110 \rangle_\beta$ crystallographic orientation of tensile stress [32]. The Young's modulus is only about 35 GPa in the $\langle 001 \rangle_\beta$ orientation, while in other orientations it can be twice as high. For example, it is about 75 GPa in $\langle 111 \rangle_\beta$ and 55 GPa in the $\langle 110 \rangle_\beta$ orientation [32,33]. This all underscores the importance of crystallographic texture in polycrystalline alloys.

Thermomechanical treatment (TMT), which includes cold plastic deformation and post-deformation annealing (PDA), is an effective method for controlling the grain and subgrain structure [34,35]. The effect of TMT conditions on the structure and functional properties varies depending on alloy composition. For Ti-Zr-Nb SMAs, certain regularities have been established regarding the effect of TMT on their structure and properties. Thus, moderate cold plastic deformation with true strain $e = 0.3$, followed by PDA at 600 °C for 30 min, creates a nanosubgrained structure in the β -phase of the Ti-22Nb-6Zr SMA and leads to the best combination of functional properties: low Young's modulus, low residual strain accumulation, good superelasticity, and high cycling stability at human body temperature [29]. However, for the Ti-18Zr-15Nb SMA, the best combination of functional properties corresponds to post-deformation annealing at 550 °C for 30 min, while annealing at 600 °C leads to recrystallization, grain growth, and the deterioration of functional properties [24,25]. Additionally, there was an attempt to obtain not only a nanosubgrained structure, but a predominantly nanograined structure in Ti-18Zr-15Nb by the implementation of severe plastic deformation with $e = 3.0$; however, the functional properties were not extensively studied [28]. As for the relatively new Ti-41Zr-12Nb SMA, the effect of TMT on its structure and functional properties has not yet been studied, and only some standard thermomechanical treatment routes have been used [19,26]. Consequently, there is lack of systematic studies of TMT effects on the structure formation and functional properties of Ti-Zr-Nb SMAs across a wide composition range.

Therefore, this work provides a comprehensive comparative study on the effect of thermomechanical treatment, including cold rolling (CR) with various strains ranging from moderate to severe and subsequent post-deformation annealing (PDA), on the phase and

structure states, crystallographic texture, and crystallographic limit of recovery strain of low-, medium-, and high-Zr Ti-Zr-Nb SMAs. It is important to note that this work does not include studying the effect of TMT on the mechanical and functional properties of Ti-Zr-Nb SMAs. The structure–property relationships essential for application will be established in future studies.

2. Materials and Methods

Ti-22Nb-6Zr, Ti-18Zr-15Nb, and Ti-41Zr-12Nb (at.%) SMAs were chosen as target materials for a comprehensive study of TMT effects on structure formation. Laboratory-size 250 g ingots were obtained by vacuum arc melting with a non-consumable tungsten electrode in an Arcasr arc200 furnace (Arcast Inc., Oxford, ME, USA). To improve the quality and homogeneity of the ingots, each was obtained with six consequent re-melts. The composition of the main elements was checked by EDS analysis on a Tescan Vega3 SBH microscope (TESCAN, Brno, Czech Republic): all elements were near the target composition within the method’s sensitivity range (Table 1). Impurity contents were measured by a high-temperature gas extraction technique using a TC-600 analyzer (Leco, Geleen, The Netherlands). All the ingots had a low impurity content, with the highest impurity contents being (wt.%) O— $0.1700 \pm 0.0020\%$, N— 0.001% , H— $0.0050 \pm 0.0004\%$, and C— $0.027 \pm 0.002\%$.

Table 1. Chemical composition of the obtained ingots from the EDS analysis (at. %).

Alloy (Designation)	Ti	Zr	Nb
Ti-22Nb-6Zr (22-6)	Main	22.1	6.3
Ti-18Zr-15Nb (18-15)	Main	18.4	15.2
Ti-41Zr-12Nb (41-12)	Main	41.2	12.2

To remove the cast structure and improve the composition homogeneity, all ingots were cut using EDM into $55 \times 10 \times 65 \dots 70$ mm billets and subjected to hot rolling with a true strain of $e = 0.3$ at $900 \text{ }^\circ\text{C}$ for the 22-6 and 18-15 alloys, and at $600 \text{ }^\circ\text{C}$ for the 41-12 alloy. Before the hot rolling, the billets were heated for 30 min at rolling temperature in an air atmosphere. The specific rolling temperature for the 41-12 alloy was selected in an attempt to minimize oxidation due to the high reactivity of zirconium. After the hot deformation, all alloys were homogenization-annealed at $900 \text{ }^\circ\text{C}$ for 30 min in an argon atmosphere and then water-quenched. The resulting alloy microstructures are shown in Figure 1. After casting, the alloys have coarse grains with a size up to $1000 \text{ }\mu\text{m}$, which can be elongated in the crystallization direction and then deformed by hot rolling. The hot rolling and subsequent homogenization annealing start the polygonization and recrystallization processes. The 22-6 alloy, after such treatment, exhibits a recrystallized structure with a grain size from 70 to $150 \text{ }\mu\text{m}$ with traces of the as-cast grain boundaries (Figure 1a). Such traces are almost invisible in the 18-15 alloy, whose structure consists of recrystallized grains ranging from 50 to $250 \text{ }\mu\text{m}$ and not-yet-recrystallized areas (Figure 1b). In 41-12, the initial grains are still presented, and some new grain boundaries are visible inside them, indicating the beginning of the recrystallization process. The recrystallized grains have sizes ranging from 20 to $100 \text{ }\mu\text{m}$ (Figure 1c).

Next, the alloys were subjected to TMT, which included CR and PDA, to form different grain structure states. These states had an average β -phase grain size of less than $1 \text{ }\mu\text{m}$ (ultrafine-grained structures), 1 to $5 \text{ }\mu\text{m}$ (fine-grained structures), or approximately $10 \text{ }\mu\text{m}$ or more (coarse-grained structures). The billets were then cut using EDM into plates with thicknesses of 0.75 , 1.5 , and 10 mm . The choice of these plate thicknesses was to ensure a uniform specimen thickness of 0.5 mm for all CR strains. The plates were subsequently cold-rolled with true strains $e = 0.3$, 1.5 , and 3.0 . They were annealed at 550 – $800 \text{ }^\circ\text{C}$ for 5 – 30 min in an argon atmosphere and then water-cooled. The processing routes for the

studied alloys are presented in Table 2. The selection of deformation strains was based on the previous work conducted on 18-15 [25].

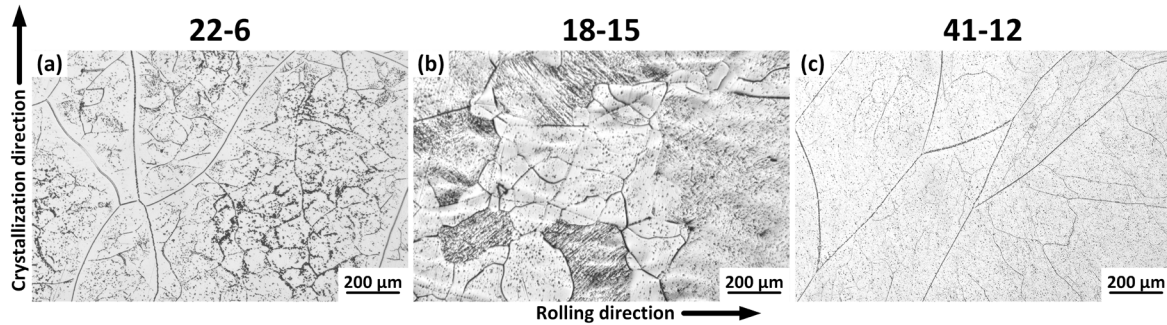


Figure 1. Microstructures of 22-6 (a), 18-15 (b), and 41-12 (c) alloys after hot rolling and homogenization annealing.

Table 2. Processing routes for the studied alloys.

CR Degree	Deformation Value	PDA	TMT Designation
Moderate	$e = 0.3$	600 °C, 30 min	0.3 + 600 (30)
		800 °C, 30 min	0.3 + 800 (30)
Intermediate	$e = 1.5$	600 °C, 30 min	1.5 + 600 (30)
		800 °C, 30 min	1.5 + 800 (30)
Severe	$e = 3.0$	550 °C, 5 min	3.0 + 550 (5)
		600 °C, 5 min	3.0 + 600 (5)
		600 °C, 30 min	3.0 + 600 (30)

After the TMT, plates of 22-6, 18-15 and 41-12 alloys were cut using EDM into specimens for structure, phase composition, and texture analyses. The 41-12 alloy had significant etching difficulties after some thermomechanical treatments. Therefore, electron backscattered diffraction (EBSD) was chosen for the analysis of grain structures with grain sizes larger than 1 μm , while transmission electron microscopy was chosen for grain structures smaller than 1 μm .

To determine the phase state before and after all TMT routes and the crystallographic limit of recovery strain (ϵ_r^{max}), X-ray diffraction analysis (XRD) was carried out at RT using 8 mm \times 10 mm specimens and a DRON-4 diffractometer (Russia) with $\text{CuK}\alpha$ radiation in the 30–90 deg 2θ range. Specimens were mechanically ground down with P1200 abrasive paper and chemically etched in a 1HF:3HNO₃:6H₂O solution to remove the oxidized and mechanically damaged layer. The lattice parameter a_β of the BCC β -phase was calculated using Nelson–Riley extrapolation. To determine the ϵ_r^{max} , specimens were additionally cold-rolled with a true strain of $e = 0.3$ to induce and stabilize the orthorhombic α'' -phase. The maximum $\beta \leftrightarrow \alpha''$ martensitic transformation lattice strain, i.e., the maximum crystallographic recovery strain limit, ϵ_r^{max} , was calculated from (020) α'' and {110} $_\beta$ peak positions following the methodology of [19], as follows:

$$\epsilon_r^{max} = \frac{b_{\alpha''} - \sqrt{2}a_\beta}{\sqrt{2}a_\beta}, \quad (1)$$

The EBSD study was performed on 10 mm \times 10 mm specimens using the FEI Scios DualBeam system (Thermo Fisher Scientific, Waltham, MA, USA). For EBSD mapping, the beam voltage and current were equal to 30 kV and 3.2 nA. The orientation maps were calculated using TSL OIM data collection software V.8 and then processed by TSL Oim Analysis software 7.2.1. Specimens were mechanically ground down with P4000 abrasive paper, polished with 0.5 μm SiO₂ suspension, and etched with Kroll's solution.

TEM was performed using a JEM-2100 transmission electron microscope (JEOL, Tokyo, Japan) at 200 kV. Specimens of 5 mm × 5 mm size were chemically etched in 1HF:3HNO₃:6H₂O solution down to 0.1 mm and then thinned on a PIPS II Gatan ion-thinning device (Gatan, Pleasanton, CA, USA).

Based on the images obtained by EBSD and TEM, the true average grain size \bar{D} , of the β -phase was measured by the random linear intercept method using at least 100 grains for calculation [36]. Since high-angle ($\geq 15^\circ$) boundaries were used in this method, some deformed areas of the initial grains with some possible internal substructures or high dislocation densities were also involved in the calculations.

3. Results and Discussion

3.1. Phase Composition after TMT

X-ray diffractograms of all the alloys after TMT are shown in Figure 2. In all cases, the main phase constituent is the BCC β -phase. In the 18-15 alloy after 3.0 + 600 (30) and in the 41-12 alloy after 1.5 + 600 (30), 1.5 + 800 (30), and 3.0 + 550 (5), a weak peak at $(130)\alpha''$ is visible (Figure 2i,l,o,t). Since it is only one peak and it does not have a systematic appearance, it can be attributed to traces that were not completely removed by etching the α'' -martensite, which were strain-induced upon mechanical polishing. Weak peaks of the α -phase are observed in the 22-6 and 18-15 alloys after severe CR and PDA at 550 °C for 5 min: there is a weak $\{110\}_\alpha$ peak in the first alloy and clearly visible $\{100\}_\alpha$, $\{101\}_\alpha$, $\{102\}_\alpha$, $\{110\}_\alpha$, and $\{112\}_\alpha$ peaks in the second one (Figure 2m,n). This could be a result of the short-term and low-temperature annealing of the well-developed nanocrystalline structure formed as a result of severe plastic deformation. Observations confirming an increase in temperature and/or changes in the kinetics of the $\beta \rightarrow \alpha$ transformation in Ti-18Zr-(14–15)Nb alloys subjected to severe CR were previously reported in [25]. Furthermore, significant changes in the ratios of β -phase line intensities can be observed due to the high variability of their crystallographic textures, necessitating additional attention.

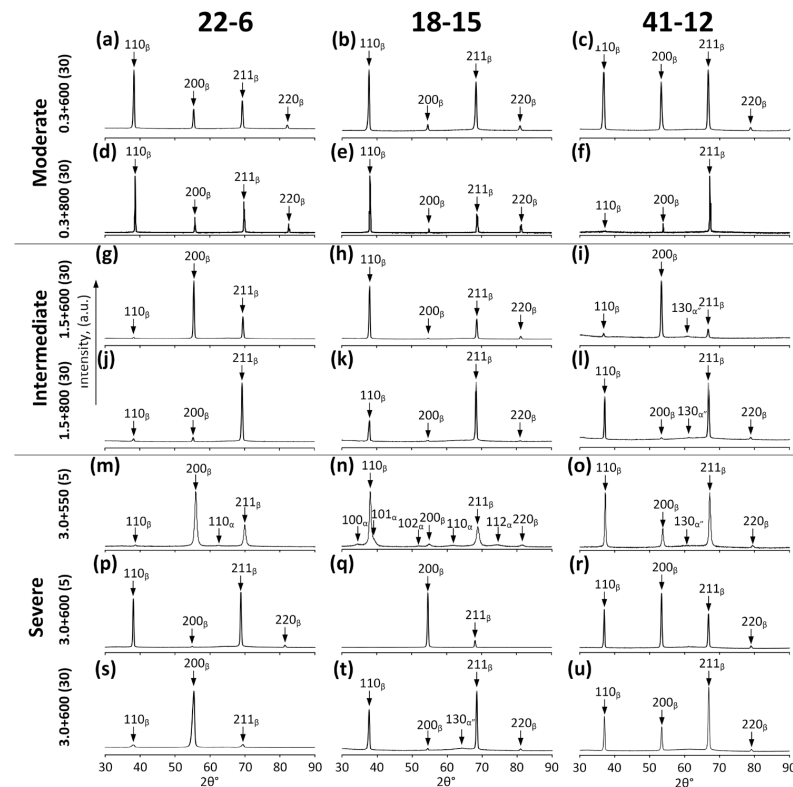


Figure 2. X-ray diffractograms of 22-6 (a,d,g,j,m,p,s), 18-15 (b,e,h,k,n,q,t), and 41-12 (c,f,i,l,o,r,u) alloys after 0.3 + 600 (30) (a–c), 0.3 + 800 (30) (d–f), 1.5 + 600 (30) (g–i), 1.5 + 800 (30) (j–l), 3.0 + 550 (5) (m–o), 3.0 + 600 (5) (p–r), and 3.0 + 600 (30) (s–u).

To evaluate the influence of the TMT on the crystal lattice structure of the β -phase, the lattice parameter a_β is calculated from each obtained X-ray diffractogram and presented in Figure 3a. It can be seen that the obtained a_β values are typical for each alloy and do not depend on the TMT within each alloy composition. The full width at half maximum (FWHM) (B_{hkl}) is measured for the $\{211\}_\beta$ X-ray line since it is the only line where the profile is clearly visible after each TMT. Figure 3b shows that the B_{211} values for all three alloys, after similar TMTs, are very close within the error limits. After 0.3 + 600 (30) TMT, all alloys exhibit a systematic increase in B_{211} . This could be a result of incomplete recrystallization when compared to 0.3 + 800 (30), which leads to complete recrystallization. The transition to intermediate CR does not increase the B_{211} value after PDA at temperatures of 600 or 800 °C. This can be explained by the earlier start of the recrystallization processes after higher CR strain due to higher accumulated strain energy. The transition to severe plastic deformation results in broadening of the $\{211\}_\beta$ peak, which is most pronounced after 3.0 + 550 (5) and 3.0 + 600 (5). Such low annealing temperatures and short times can result in the formation of ultrafine-grained structures which in turn increase the FWHM [25].

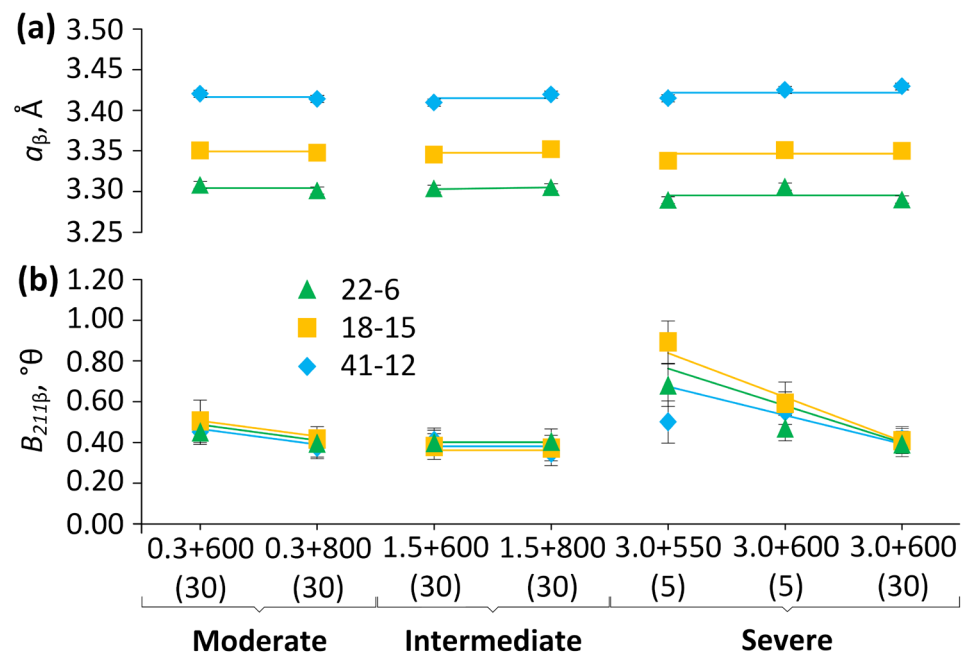


Figure 3. Changes in the lattice parameter a_β (a) and $\{211\}_\beta$ FWHM B (b) of β -phase of 22-6, 18-15, and 41-12 alloys after 0.3 + 600 (30), 0.3 + 800 (30), 1.5 + 600 (30), 1.5 + 800 (30), 3.0 + 550 (5), 3.0 + 600 (5), and 3.0 + 600 (30).

3.2. Microstructure Characterization after TMT

3.2.1. Scanning Electron Microscopy

The EBSD images shown in Figure 4 demonstrate the alloy microstructures after 0.3 + 600 (30), 0.3 + 800 (30), 1.5 + 600 (30), 1.5 + 800 (30), and 3.0 + 600 (30) TMTs.

In all alloys, after 0.3 + 600 (30), a “plate” structure within the grain body of the β -phase is observed. This microstructure feature is a result of $\{332\}\langle 113 \rangle$ twinning during CR, which has been extensively studied for various metastable titanium alloys. The extent of cold plastic deformation greatly influences its contribution to microstructure formation [37–40]. Subsequent PDA at 600 °C does not eliminate the twinning structure through static recrystallization. Only in the 18-15 alloy is the formation of new β -phase grains with a size of 2–10 μm locally observed (see Figure 4b), indicating a partial recrystallization. The twinned structures of the 22-6 and 41-12 alloys remain preserved and are more resistant to recrystallization during PDA at 600 °C (see Figure 4a,c). The extent of cold plastic deformation greatly influences its contribution to microstructure formation (see Figure 4a).

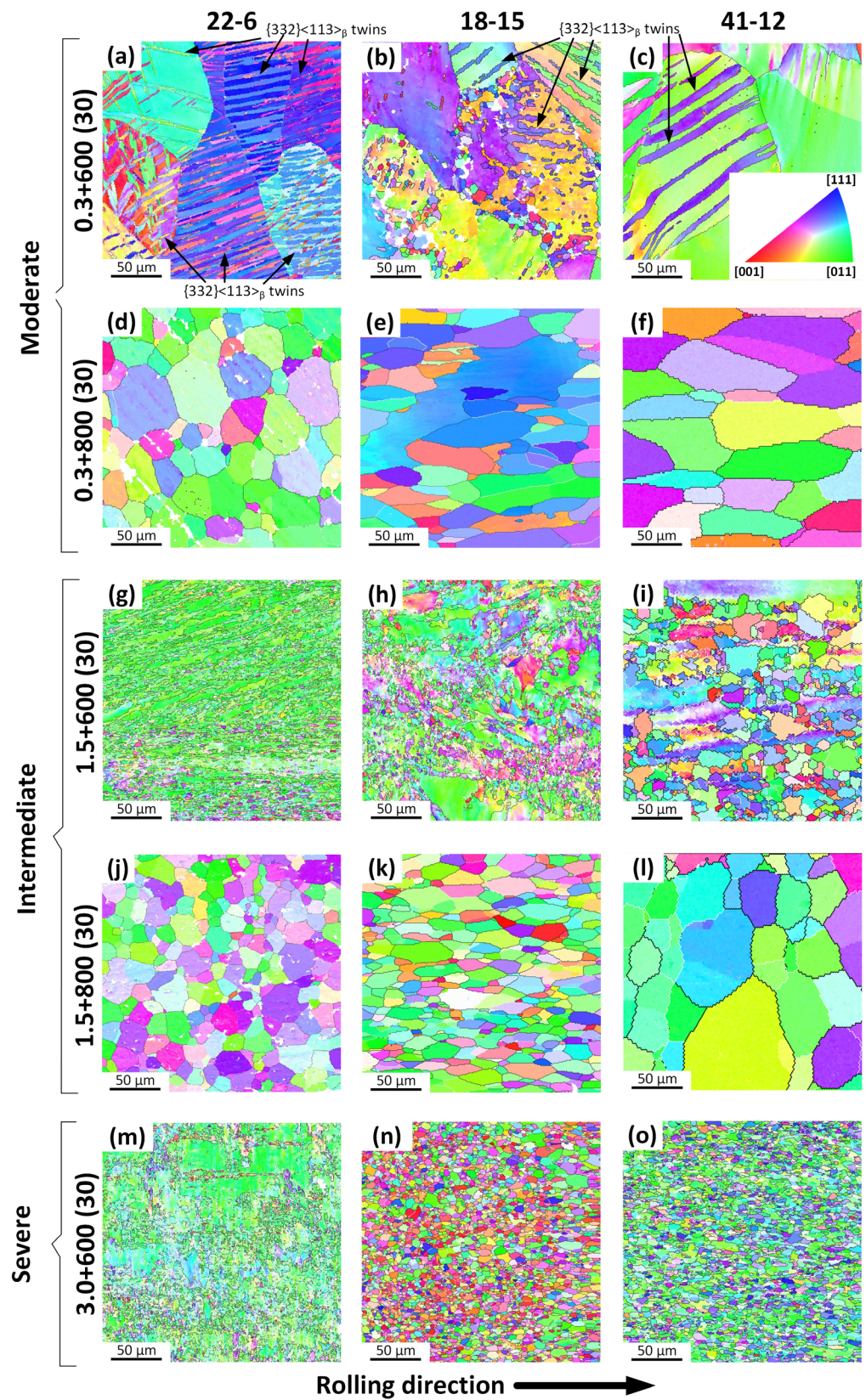


Figure 4. Orientation distribution maps (EBSD images) of 22-6 (a,d,g,j,m), 18-15 (b,e,h,k,n), and 41-12 (c,f,i,l,o) alloys after 0.3 + 600 (30) (a–c), 0.3 + 800 (30) (d–f), 1.5 + 600 (30) (g–i), 1.5 + 800 (30) (j–l), and 3.0 + 600 (30) (m–o). Black lines correspond to high-angle boundaries ($\geq 15^\circ$); white lines correspond to low-angle boundaries ($< 15^\circ$).

Increasing the PDA temperature to 800 °C leads to the development of recrystallization and grain growth in all alloys (Figure 4d–f). However, in the 18-15 and 41-12 alloys, the grains are elongated in the rolling direction, indicating the development of recrystallization through the predominantly directed movement of high-angle boundaries. A similar phenomenon was previously observed in the 18-15 alloy as a result of annealing after hot rotary forging [41]. This phenomenon deserves a separate study. TMT including 1.5 + 600 (30) leads to the formation of a mixed partially recrystallized microstructure of the β -phase characterized by a combination of smaller equiaxed recrystallized grains with non-recrystallized areas which presumably contain a polygonized dislocation substructure, i.e., subgrains separated by low-angle boundaries (Figure 4g–i). After PDA at 800 °C, predominantly recrystallized grains are observed. It should be noted that the size of the structure elements increases with the transition from low- to high-Zr alloys; however, there are non-recrystallized areas in the alloys (Figure 4j–l).

The use of 3.0 + 600 (30) TMT leads to significant grain refinement in all alloys (Figure 4m–o). Based on the EBSD maps, the histograms of grain size distribution were plotted (Figure 5). For microstructures containing elongated structure elements, grain sizes were measured in two directions: the rolling direction and the transversal direction. For equiaxed grains, these values were equal within the error limits, and only one value of the grain size is given as an average of the values in two directions.

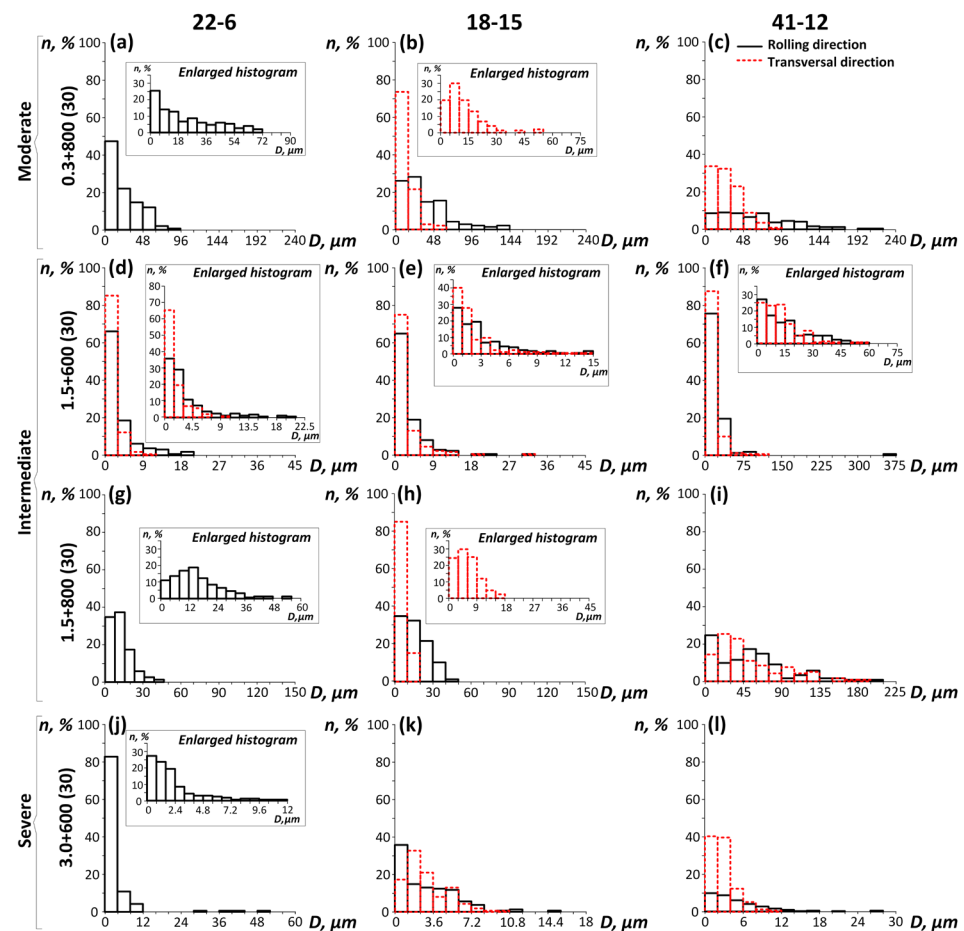


Figure 5. Grain size D distribution histograms of 22-6 (a,d,g,j), 18-15 (b,e,h,k), and 41-12 (c,f,i,l) alloys after 0.3 + 800 (30) (a–c), 1.5 + 600 (30) (d–f), 1.5 + 800 (30) (g–i), and 3.0 + 600 (30) (j–l).

Almost all grain size D distribution histograms for the 22-6, 18-15, and 41-12 alloys closely resemble the log-normal distribution, with a bias towards the smaller grains. This bias is a result of the recrystallization process, when a number of new smaller grains occupy the large, deformed areas. Thus, some histograms even show bars that extend beyond

the main histogram towards larger grain sizes: in the 22-6 alloy after 3.0 + 600 (30) and in the 18-15 and 41-12 alloys after 1.5 + 600 (30) (Figure 5d,f,j). This is a result of counting some non-recrystallized deformed areas in the initial grains; therefore, this means that recrystallization is not completed after such treatments. Such incomplete recrystallization can also be a result of a non-uniform initial deformation, i.e., when highly deformed areas recrystallize first, while less deformed areas are still not recrystallized. In 41-12, after 1.5 + 800 (30), the histogram manifests more than one pronounced peak, which could be a result of the secondary recrystallization process, when some grains grow at the expense of other grains (Figure 5i). Some histograms of grain size distribution demonstrate a metallographic texture with elongation in the initial rolling direction: in 18-15 and 41-12 after 0.3 + 800 (30); in 22-6 after 1.5 + 600 (30); in 18-15 after 1.5 + 800 (30); and in the 18-15 and 41-12 alloys after 3.0 + 600 (30) (Figure 5b–d,h,k,l).

3.2.2. Transmission Electron Microscopy

Since the grain structure after 3.0 + 550 (5) and 3.0 + 600 (5) was too fine for the EBSD system that we used, TEM analysis of the structure was performed. Figure 6 presents the TEM bright- and dark-field images, along with the corresponding SAED patterns. The obtained TEM images exhibit an ultrafine-grained submicrocrystalline structure of the β -phase. An exception is the SAED pattern of the 18-15 alloy, where reflections of the α -phase are present after 3.0 + 550 (5) (Figure 6b), which confirms the results of the XRD analysis (Figure 2). The TEM images show that after annealing at 550 and 600 °C for 5 min, the low-angle misorientations are still preserved with a predominance of high-angle boundaries. The high-angle boundaries (Figure 6) are confirmed by the high-angle azimuthal misorientations in the selected area electron diffraction (SAED) patterns and the observation of individual grains in the dark-field (DF) images. However, some internal low-angle boundaries can also be seen in the dark-field images of all alloys. These subboundaries divide grains surrounded by high-angle boundaries into subgrains (Figure 6a–f). Thus, after 3.0 + 550 (30) and 3.0 + 600 (30) TMT, a mixed submicrograined and submicrosubgrained structure of the β -phase with a grain/subgrain size in the 100 to 1000 nm range is formed.

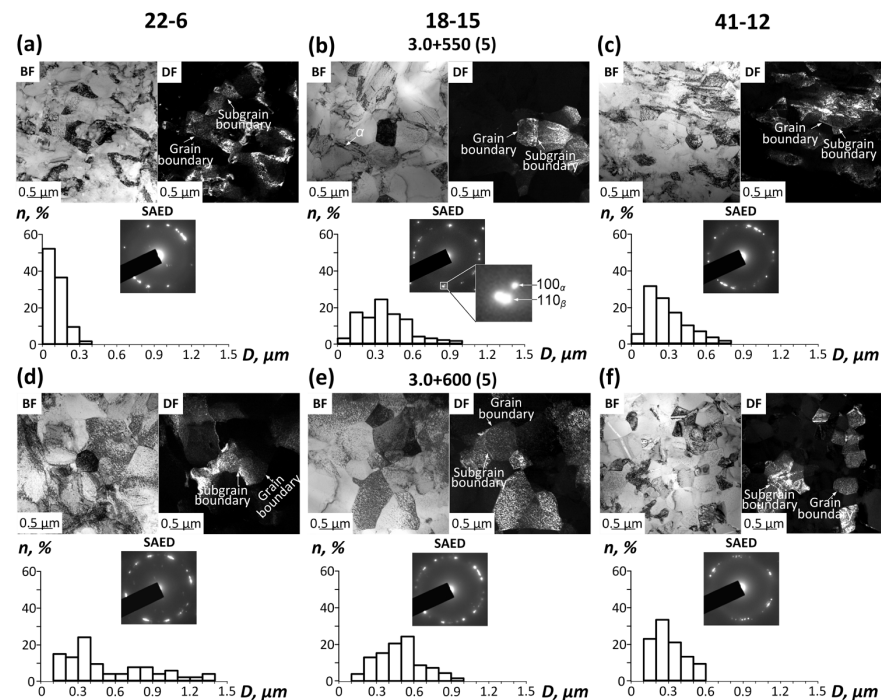


Figure 6. TEM images of 22-6 (a,d), 18-15 (b,e), and 41-12 (c,f) alloys after 3.0 + 550 (5) (a–c) and 3.0 + 600 (5) (d–f).

Based on the bright-field images, grain/subgrain histograms (i.e., without separation into grain and subgrain size distributions) were built (see Figure 6) and the average grain size \bar{D} , was calculated and compared with \bar{D} , (calculated for other TMT routes in Figure 7). The histograms of all alloys exhibit a log-normal distribution with a single peak, except for one 22-6 alloy after 3.0 + 600 (5), which does not follow a log-normal distribution. This deviation can be attributed to non-uniform recrystallization due to non-uniform initial deformation.

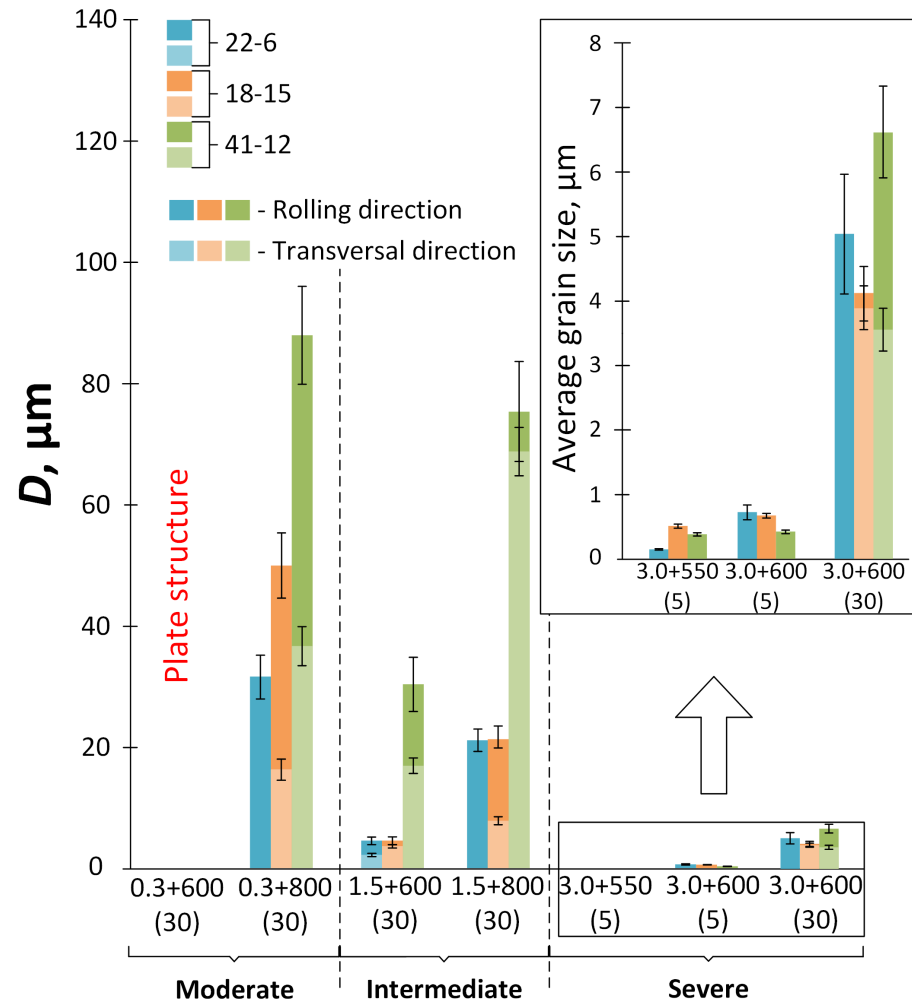


Figure 7. Average grain size \bar{D} , histograms of 22-6, 18-15, and 41-12 alloys in the initial states and after 0.3 + 600 (30), 0.3 + 800 (30), 1.5 + 600 (30), 1.5 + 800 (30), 3.0 + 550 (5), 3.0 + 600 (5), and 3.0 + 600 (30).

It can be observed in Figure 4 that 0.3 + 600 (30) TMT leads to the formation of a plate structure of the β -phase where the calculation of grain size \bar{D} , is not possible. Increasing the PDA temperature to 800 °C leads to a recrystallized structure in all alloys. In 22-6, however, an equiaxed grain structure forms with an average size of $31.8 \pm 3.6 \mu\text{m}$, while in 18-15 and 41-12, an elongated structure forms with average grain sizes \bar{D} , of $\sim 50.1 \pm 5.4 \times 16.5 \pm 1.8 \mu\text{m}$ and $88.0 \pm 8.1 \times 36.9 \pm 3.1 \mu\text{m}$, respectively (Figures 4 and 7). The decrease in grain size \bar{D} , in all alloys after PDA at 800 °C, compared to the initial state, is associated with the occurrence of static recrystallization [24].

Intermediate 1.5 + 600 (30) creates a predominantly fine-grained structure with an average grain size of $4.5 \pm 0.6 \times 2.1 \pm 0.3 \mu\text{m}$ for 22-6, $4.5 \pm 0.6 \times 3.5 \pm 0.5 \mu\text{m}$ for 18-15, and $30.2 \pm 4.4 \times 16.3 \pm 2.1 \mu\text{m}$ for 41-12. It consists of a mixture of recrystallized equiaxed grains and non-recrystallized grains (containing a polygonized dislocation substructure due to static polygonization) (Figure 4). After 1.5 + 800 (30) TMT, a fully statically recrystallized

fine-grained structure in 22-6 and 18-15 and a coarse-grained structure in 41-12 are formed. The average equiaxed grain sizes are $21.4 \pm 1.9 \mu\text{m}$ for 22-6 and $75.1 \pm 8.2 \times 68.36 \pm 7.7 \mu\text{m}$ for 41-12, and the average elongated grains sizes are $21.5 \pm 1.8 \times 8.1 \pm 0.7 \mu\text{m}$ for 18-15.

After severe 3.0 + 550 (5), a predominantly ultrafine-grained recrystallized equiaxed structure of the β -phase is formed with an average grain size of $0.15 \pm 0.01 \mu\text{m}$ in 22-6, $0.51 \pm 0.03 \mu\text{m}$ in 18-15, and $0.38 \pm 0.03 \mu\text{m}$ in the 41-12 alloy. An increase in PDA temperature to $600 \text{ }^\circ\text{C}$ (5 min) leads to the grain growing to $0.73 \pm 0.11 \mu\text{m}$ in 22-6, $0.68 \pm 0.04 \mu\text{m}$ in 18-15, and $0.43 \pm 0.03 \mu\text{m}$ in the 41-12 alloy. However, all grain structures still remain predominantly in the ultrafine size range. A subsequent increase in PDA time at $600 \text{ }^\circ\text{C}$ to 30 min creates a fine-grained structure with an average size of $5.0 \pm 0.9 \mu\text{m}$ for 22-6, $4.1 \pm 0.4 \times 3.9 \pm 0.3 \mu\text{m}$ for 18-15, and $6.6 \pm 0.7 \times 3.6 \pm 0.3 \mu\text{m}$ for the 41-12 alloy. In 22-6, the fine-grained structure is almost equally combined with non-recrystallized areas with some substructures inside, which is a result of non-uniform deformation during rolling.

In summarizing the analysis results of the grain structures of these alloys, we consider the following limitations. Firstly, in ternary alloys, the separate effect of an individual alloying element on grain size cannot be determined because the Nb and Zr content changes are simultaneous yet disproportionate. Secondly, due to the broad range of grain sizes, different methods were used to study structural element sizes. Taking into account the above limitations and analyzing the results obtained, the following obvious features can be noticed: (1) an increase in the degree of cold plastic deformation from intermediate to severe leads to intensive grain refinement by 3–3.5 times in high-zirconium alloys; (2) a decrease in the PDA temperature from 800 to $600 \text{ }^\circ\text{C}$ (30 min) leads to grain refinement by 1.1 to 2.2 times from low- to high-Zr alloys.

3.3. Crystallographic Texture Analysis

Figure 8 shows the inverse pole figures plotted for the rolling (RD) and normal (ND) directions with intensity scales calculated from the EBSD images in Figure 4. In all alloys after 0.3 + 600 (30), β -phase grains do not have any preferential crystallographic orientation in any of the presented directions (Figure 8a–c). This lack of orientation may be due to the formation of the twinned structure and the corresponding texture being blurred. Increasing the PDA temperature of the 22-6 alloy to $800 \text{ }^\circ\text{C}$ promotes the formation of a weak $\{111\}_\beta \langle 110 \rangle_\beta$ recrystallization texture, which is confirmed by the maximum intensities in $\langle 110 \rangle_\beta \parallel \text{RD}$ and $\langle 111 \rangle_\beta \parallel \text{ND}$ (Figure 8d) [30,42]. In other alloys, no such features are observed after 0.3 + 800 (30), and the distribution of crystallographic orientations appears random (Figure 8e,f). This difference in crystallographic texture formation may be associated with the transition from low- to high-Zr alloys, and may be associated with increased Nb content (22-6 alloy), which aligns with the findings reported in [42]. Changes in crystallographic texture resulting from 1.5 + 600 (30) support this hypothesis. A strong $\{111\}_\beta \langle 110 \rangle_\beta$ crystallographic texture is formed in the 22-6 alloy after 1.5 + 600 (30) (Figure 8g). In the 18-15 alloy, this same texture is weaker (Figure 8h). However, in the 41-12 alloy, this type of texture is not fully formed (Figure 8i), which is probably due to the partial development of recrystallization. This is confirmed by the fact that after 1.5 + 800 (30), a strong $\{111\}_\beta \langle 110 \rangle_\beta$ recrystallization texture is formed in the high-Zr alloy (Figure 8l). For the 22-6 and 18-15 alloys, increasing the PDA temperature from 600 to $800 \text{ }^\circ\text{C}$ after intermediate CR does not lead to noticeable changes in the crystallographic texture (Figure 8j,k). After severe CR and PDA at $600 \text{ }^\circ\text{C}$ in all alloys, a strong $\{111\}_\beta \langle 110 \rangle_\beta$ recrystallization texture is formed (Figure 8m–o), which is consistent with studies conducted on Ti-Nb- and Ti-Zr-based SMAs presented in [7,32,43–45]. It is important to note that when transitioning from high-Zr alloys to low-Zr alloys, along with a combined increase in Nb content from 12 to 22 at.%, the intensity of the maxima on the inverse pole figures increases (Figure 8m–o). This confirms the enhancement in the crystallographic texture. In summary, the low-Zr alloys are more susceptible to the formation of a favorable $\{111\}_\beta \langle 110 \rangle_\beta$ recrystallization texture during TMT. This formation requires a lower degree of deformation by CR, and its

intensity increases more significantly with an increasing degree of deformation compared to alloys with a higher Zr content.

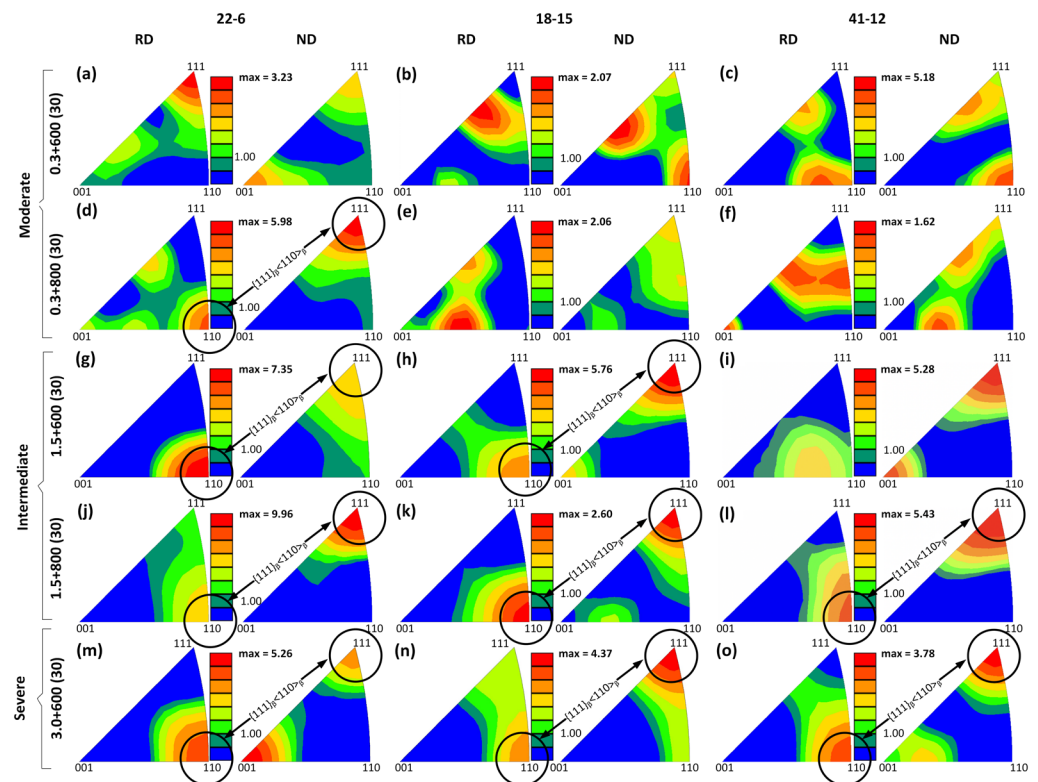


Figure 8. Inverse pole figures plotted in the RD and ND of 22-6 (a,d,g,j,m), 18-15 (b,e,h,k,n), and 41-12 (c,f,i,l,o) alloys after 0.3 + 600 (30) (a–c), 0.3 + 800 (30) (d–f), 1.5 + 600 (30) (g–i), 1.5 + 800 (30) (j–l), and 3.0 + 600 (30) (m–o).

3.4. Crystallographic Limit of Recovery Strain

It was previously reported in [46] that grain refinement down to a nanometer-scaled grain size and the development of a dislocation substructure in the parent B2-phase in Ti-Ni SMAs significantly reduce the crystallographic limit of recovery strain (ϵ_r^{max}). Thus, it was of interest to compare the effect of grain size on the crystallographic limit of recovery strain of the studied Ti-Nb-Zr alloys, particularly as this effect had not yet been studied in nickel-free Ti-based SMAs. All alloys after TMT were selected for the study and grain structures were graded into three ranges: coarse-grained after 1.5 + 800 (30); fine-grained after 1.5 + 600 (30); and ultrafine-grained structure after 3.0 + 600 (5) and 3.0 + 550 (5). Specimens of these alloys which contained predominant parent β -phases after TMT were subjected to additional CR with $e = 0.3$ to produce a stress-induced α'' -martensite that was thermally stabilized by cold plastic deformation. The corresponding fragments of the X-ray diffractograms are shown in Figure 9.

Since there are not enough α'' -phase lines with well-measured positions to use a conventional least-squares method to calculate the lattice parameters and consequently the crystallographic limit of recovery strain with a representative accuracy, a direct calculation is used based on the $(020)_{\alpha''}$ and $\{110\}_{\beta}$ peak positions, as in [19]. All alloys after TMT at 3.0 + 550 (5) (Figure 9j–l) had their smallest average true grain size (\bar{D}); however, after additional CR, the 18-15 alloy (Figure 9k) did not form enough α'' -phases with clearly visible $(020)_{\alpha''}$ X-ray lines to calculate the crystallographic limit of the recovery strain (ϵ_r^{max}), the more so, it was overlapped by a stronger $\{100\}_{\alpha}$ line. Therefore, the 3.0 + 600 (5) route was chosen to calculate the crystallographic resource of recovery strain in the ultrafine-grained structure of the β -phase (Figure 9g–i).

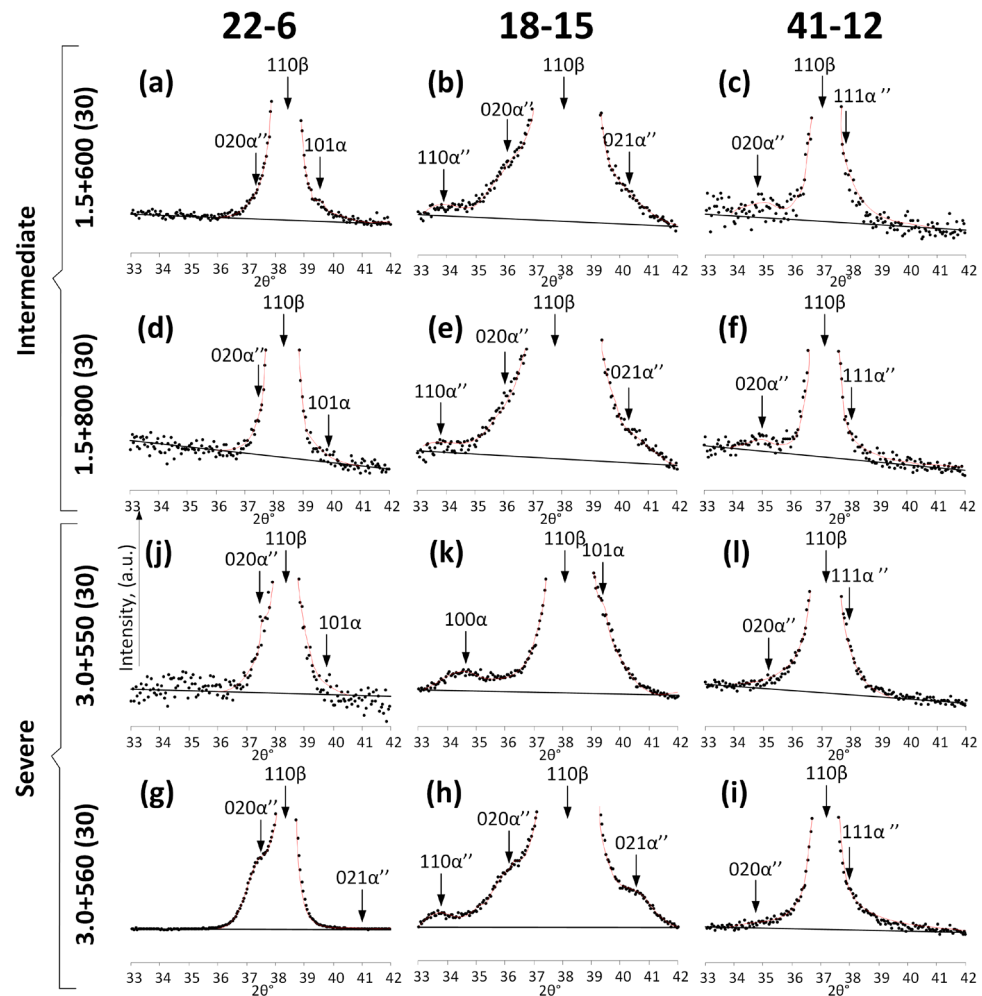


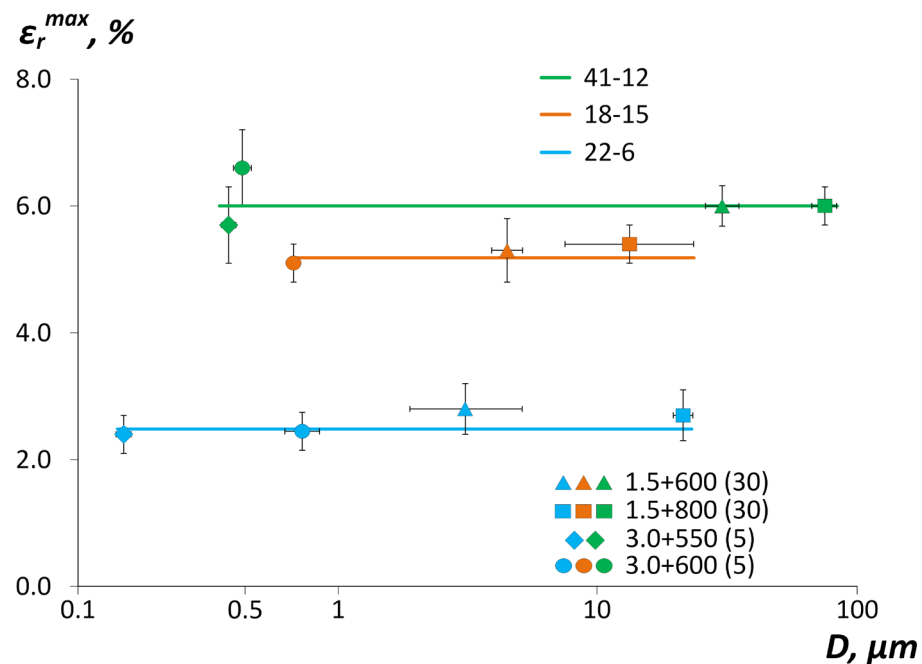
Figure 9. X-ray diffractograms of 22-6 (a,d,g,j), 18-15 (b,e,h,k), and 41-12 (c,f,i,l) alloys subjected to stabilizing cold rolling after 1.5 + 600 (30) (a–c), 1.5 + 800 (30) (d–f), 3.0 + 550 (5) (j–l), and 3.0 + 600 (5) (g–i).

Based on the $(020)_{\alpha''}$ and $\{110\}_{\beta}$ peak positions, the interplanar distances of $d_{020\alpha''}$ and $d_{110\beta}$ and the crystallographic limit of recovery strain (ε_r^{max}) were calculated for the studied Ti-Nb-Zr alloys (Table 3).

The 41-12 alloy in the coarse-grained state exhibits the highest crystallographic limit of recovery strain of $\varepsilon_r^{max} \approx 6\%$. This value is considered high for nickel-free SMAs. The transition from high- to low-Zr and low- to high-Nb alloys leads to a pronounced decrease in the ε_r^{max} value to $\approx 5\%$ for the 18-15 alloy and to $\approx 3\%$ for the 22-6 alloy. These results correlate well with the literature data [19,24,25]. Decreases in grain size and the transition to the ultrafine-grained structure of the β -phase do not affect the crystallographic limit of recovery strain (Figure 10). The trend of a decreasing crystallographic limit of recovery strain with grain refinement is well known in Ti-Ni SMAs [46]. However, this has been reported for grain sizes close to 100 nm (0.1 μm) and below. In contrast, in the current study, all alloys had larger minimum average grain sizes: $0.15 \pm 0.01 \mu\text{m}$ for 22-6, $0.68 \pm 0.04 \mu\text{m}$ for 18-15, and $0.38 \pm 0.03 \mu\text{m}$ for the 41-12 alloy. Therefore, in future research, the impact of grain size dependence on the crystallographic limit of recovery strain in Ti-Zr-Nb SMAs needs to be confidently verified.

Table 3. Crystallographic limit of recovery strain depending on the composition of the Ti-Zr-Nb alloys and the grain size.

Thermomechanical Treatment	\bar{D} , μm	ϵ_r^{max} , %
22-6		
1.5 + 600 (30)	$2.14 \pm 0.26 \times 4.47 \pm 0.61$	2.9 ± 0.4
1.5 + 800 (30)	21.3 ± 1.8	2.7 ± 0.4
3.0 + 550 (5)	0.15 ± 0.01	2.4 ± 0.3
3.0 + 600 (5)	0.73 ± 0.11	2.3 ± 0.3
18-15		
1.5 + 600 (30)	$3.49 \pm 0.54 \times 4.49 \pm 0.61$	5.3 ± 0.5
1.5 + 800 (30)	$8.1 \pm 0.7 \times 21.5 \pm 1.8$	5.0 ± 0.3
3.0 + 550 (5)	0.51 ± 0.03	-
3.0 + 600 (5)	0.68 ± 0.04	5.4 ± 0.3
41-12		
1.5 + 600 (30)	$16.3 \pm 2.4 \times 30.2 \pm 4.4$	6.0 ± 0.4
1.5 + 800 (30)	$68.4 \pm 7.7 \times 75.1 \pm 8.2$	6.0 ± 0.3
3.0 + 550 (5)	0.38 ± 0.03	5.7 ± 0.6
3.0 + 600 (5)	0.43 ± 0.03	6.6 ± 0.6

**Figure 10.** The influence of grain size \bar{D} on the crystallographic limit of recovery strain (ϵ_r^{max}) of 22-6, 18-15, and 41-12 alloys after 1.5 + 600 (30), 1.5 + 800 (30), 3.0 + 550 (5), and 3.0 + 600 (5).

4. Conclusions

The results of this comparative study on the effects of thermomechanical treatment—including cold rolling (CR) with various strains ranging from moderate to severe and subsequent post-deformation annealing (PDA)—on the phase and structure states, crystallographic texture, and crystallographic limit of recovery strains of low-, medium-, and high-Zr Ti-Zr-Nb SMAs have led to the following conclusions:

1. The intermediate cold rolling of Ti-22Nb-6Zr, Ti-18Zr-15Nb, and Ti-41Zr-12Nb alloys with $e = 1.5$ and PDA at 800 °C for 30 min results in the formation of fine- and coarse-grained structures. The grain size of the predominant β -phase increases in high-zirconium alloys.

2. The severe cold rolling of Ti-22Nb-6Zr, Ti-18Zr-15Nb, and Ti-41Zr-12Nb alloys with $e = 3.0$ and PDA at 550 °C for 5 min results in the formation of a recrystallized equiaxed predominantly ultrafine-grained structure of the β -phase with some low-angle boundaries inside the grains. The average grain/subgrain size \bar{D} ranges from 0.15 to 0.50 μm based on the TEM bright-field images.
3. The transition of cold rolling strain from $e = 1.5$ to $e = 3.0$ results in significant grain refinement by 3–3.5 times in high-zirconium Ti-41Zr-12Nb alloys. Moreover, a decrease in the PDA temperature from 800 to 600 °C (30 min) leads to grain refinement by 1.1 to 2.2 times from low- to high-Zr alloys.
4. After $e = 0.3 + 800$ °C for 30 min, a weak favorable $\{111\}_\beta <110>_\beta$ recrystallization texture is formed in the Ti-22Nb-6Zr alloy, while no texture is observed in the other alloys. After $e = 1.5 + 600$ °C for 30 min, the Ti-22Nb-6Zr alloy exhibits the strongest crystallographic texture $\{111\}_\beta <110>_\beta$ compared to the Ti-18Zr-15Nb alloy, where the texture is weaker, and the Ti-41Zr-12Nb alloy, where this type of texture is not completely formed due to the partial development of recrystallization. Increasing the degree of CR to severe ($e = 3.0$) leads to the formation of a strong $\{111\}_\beta <110>_\beta$ recrystallization texture after PDA in all alloys. Alloys with a low Zr content are more susceptible to this type of crystallographic texture formation during TMT, primarily due to a higher Nb content.
5. The Ti-41Zr-12Nb alloy has a highest crystallographic limit of recovery strain of $\varepsilon_r^{max} \approx 6\%$. The crystallographic limit decreases with the transition from high- to low-Zr and from low- to high-Nb alloys: $\approx 5\%$ for Ti-18Zr-15Nb and $\approx 3\%$ for the Ti-22Nb-6Zr alloy. The transition from a coarse-grained to an ultrafine-grained structure of the β -phase in the studied Ti-Zr-Nb alloys does not affect the crystallographic limit of recovery strain within the studied ranges up to 0.15 ± 0.01 μm for Ti-22Nb-6Zr, 0.68 ± 0.04 μm for Ti-18Zr-15Nb, and 0.38 ± 0.03 μm for the Ti-41Zr-12Nb alloy.

Author Contributions: A.B. (Alexandra Baranova): XRD analysis, data treatment, results interpretation, manuscript preparation and editing; S.D.: project conceptualization, results interpretation and manuscript preparation; I.V.: formal analysis, specimen manufacturing, data treatment, results interpretation, and manuscript preparation; A.B. (Andrey Bazlov) ingot production, data treatment; N.T.: TEM microscopy, data treatment; V.S.: data treatment, results interpretation, manuscript preparation; T.T.: SEM microscopy, data treatment; O.S.: formal analysis, specimen manufacturing, data treatment, results interpretation; S.P.: XRD analysis, results interpretation and editing. All authors have read and agreed to the published version of the manuscript.

Funding: The present work has been carried out with the financial support of the Russian Science Foundation, project number 21-73-10167, <https://rscf.ru/en/project/21-73-10167/> (accessed on 19 April 2024) (ingots manufacturing, thermomechanical treatment, optical microscopy, TEM and X-ray diffraction analysis) and strategic project “Biomedical materials and bioengineering” within the framework of the Strategic Academic Leadership Program “Priority 2030” at NUST “MISIS” (EBSD analysis).

Institutional Review Board Statement: Not applicable.

Informed Consent Statement: Not applicable.

Data Availability Statement: The original contributions presented in the study are included in the article, further inquiries can be directed to the corresponding author. The data are not publicly available due to privacy.

Conflicts of Interest: The authors declare no conflicts of interest.

References

1. Kim, J.; Kim, H.Y.; Inamura, T.; Hosoda, H.; Miyazaki, S. Shape Memory Characteristics of Ti–22Nb–(2–8) Zr (at.%) Biomedical Alloys. *Mater. Sci. Eng. A* **2005**, *403*, 334–339. [[CrossRef](#)]
2. Miyazaki, S.; Kim, H.Y.; Hosoda, H. Development and Characterization of Ni-Free Ti-Base Shape Memory and Superelastic Alloys. *Mater. Sci. Eng. A* **2006**, *438–440*, 18–24. [[CrossRef](#)]

3. Niinomi, M. Mechanical Biocompatibilities of Titanium Alloys for Biomedical Applications. *J. Mech. Behav. Biomed. Mater.* **2008**, *1*, 30–42. [[CrossRef](#)] [[PubMed](#)]
4. Biesiekierski, A.; Wang, J.; Abdel-Hady Gepreel, M.; Wen, C. A New Look at Biomedical Ti-Based Shape Memory Alloys. *Acta Biomater.* **2012**, *8*, 1661–1669. [[CrossRef](#)] [[PubMed](#)]
5. Bönisch, M.; Calin, M.; Waitz, T.; Panigrahi, A.; Zehetbauer, M.; Gebert, A.; Skrotzki, W.; Eckert, J. Thermal Stability and Phase Transformations of Martensitic Ti-Nb Alloys. *Sci. Technol. Adv. Mater.* **2013**, *14*, 055004. [[CrossRef](#)] [[PubMed](#)]
6. Aeby-Gautier, E.; Settefrati, A.; Bruneseaux, F.; Appolaire, B.; Denand, B.; Dehmas, M.; Geandier, G.; Boulet, P. Isothermal α'' Formation in β Metastable Titanium Alloys. *J. Alloys Compd.* **2013**, *577*, S439–S443. [[CrossRef](#)]
7. Kim, H.Y.; Fu, J.; Tobe, H.; Kim, J.; Miyazaki, S. Crystal Structure, Transformation Strain, and Superelastic Property of Ti-Nb-Zr and Ti-Nb-Ta Alloys. *Shape Mem. Superelasticity* **2015**, *1*, 107–116. [[CrossRef](#)]
8. Yang, Y.; Castany, P.; Cornen, M.; Prima, F.; Li, S.J.; Hao, Y.L.; Gloriant, T. Characterization of the Martensitic Transformation in the Superelastic Ti-24Nb-4Zr-8Sn Alloy by in Situ Synchrotron X-Ray Diffraction and Dynamic Mechanical Analysis. *Acta Mater.* **2015**, *88*, 25–33. [[CrossRef](#)]
9. Niinomi, M. *Metals for Biomedical Devices*; Woodhead Publishing: Cambridge, UK, 2019.
10. Gasik, M.M.; Yu, H. Phase Equilibria and Thermal Behavior of the Biomedical Ti-Nb-Zr Alloy. In Proceedings of the 17th Plansee Seminar, Reutte, Austria, 25–29 May 2009.
11. You, L.; Song, X. A Study of Low Young's Modulus Ti-Nb-Zr Alloys Using d Electrons Alloy Theory. *Scr. Mater.* **2012**, *67*, 57–60. [[CrossRef](#)]
12. Karre, R.; Niranjan, M.K.; Dey, S.R. First Principles Theoretical Investigations of Low Young's Modulus Beta Ti-Nb and Ti-Nb-Zr Alloys Compositions for Biomedical Applications. *Mater. Sci. Eng. C* **2015**, *50*, 52–58. [[CrossRef](#)]
13. Weng, W.; Biesiekierski, A.; Li, Y.; Wen, C. Effects of Selected Metallic and Interstitial Elements on the Microstructure and Mechanical Properties of Beta Titanium Alloys for Orthopedic Applications. *Materialia* **2019**, *6*, 100323. [[CrossRef](#)]
14. Kim, K.M.; Kim, H.Y.; Miyazaki, S. Effect of Zr Content on Phase Stability, Deformation Behavior, and Young's Modulus in Ti-Nb-Zr Alloys. *Materials* **2020**, *13*, 476. [[CrossRef](#)] [[PubMed](#)]
15. Takamura, K.; Hayashi, K.; Ishinishi, N.; Yamada, T.; Sugioka, Y. Evaluation of Carcinogenicity and Chronic Toxicity Associated with Orthopedic Implants in Mice. *J. Biomed. Mater. Res.* **1994**, *28*, 583–589. [[CrossRef](#)] [[PubMed](#)]
16. Long, M.; Rack, H.J. Titanium Alloys in Total Joint Replacement—A Materials Science Perspective. *Biomaterials* **1998**, *19*, 1621–1639. [[CrossRef](#)] [[PubMed](#)]
17. Arias-González, F.; Rodríguez-Contreras, A.; Punset, M.; Manero, J.M.; Barro, Ó.; Fernández-Arias, M.; Lusquiños, F.; Gil, F.J.; Pou, J. In-Situ Laser Directed Energy Deposition of Biomedical Ti-Nb and Ti-Zr-Nb Alloys from Elemental Powders. *Metals* **2021**, *11*, 1205. [[CrossRef](#)]
18. Nakaniwa, M.; Duerig, T.W.; Melton, K.N.; Stöckel, D.; Wayman, C.M.; Duerig, T.W.; Stockel, D.; Wayman, C.M. *Engineering Aspects of Shape Memory Alloys*; Butterworth-Heinemann: Oxford, UK, 1990.
19. Konopatsky, A.; Sheremetyev, V.; Dubinskiy, S.; Zhukova, Y.; Firestein, K.; Golberg, D.; Filonov, M.; Prokoshkin, S.; Brailovski, V. Structure and Superelasticity of Novel Zr-Rich Ti-Zr-Nb Shape Memory Alloys. *Shape Mem. Superelasticity* **2021**, *7*, 304–313. [[CrossRef](#)]
20. Baker, C. The Shape-Memory Effect in a Titanium-35 Wt.-% Niobium Alloy. *Met. Sci. J.* **1971**, *5*, 92–100. [[CrossRef](#)]
21. Abdel-Hady, M.; Hinoshita, K.; Morinaga, M. General Approach to Phase Stability and Elastic Properties of β -Type Ti-Alloys Using Electronic Parameters. *Scr. Mater.* **2006**, *55*, 477–480. [[CrossRef](#)]
22. Abdel-Hady, M.; Fuwa, H.; Hinoshita, K.; Kimura, H.; Shinzato, Y.; Morinaga, M. Phase Stability Change with Zr Content in β -Type Ti-Nb Alloys. *Scr. Mater.* **2007**, *57*, 1000–1003. [[CrossRef](#)]
23. Kim, H.Y.; Miyazaki, S. Martensitic Transformation and Superelastic Properties of Ti-Nb Base Alloys. *Mater. Trans.* **2015**, *56*, 625–634. [[CrossRef](#)]
24. Sheremetyev, V.; Lukashovich, K.; Kreitzberg, A.; Kudryashova, A.; Tsaturyants, M.; Galkin, S.; Andreev, V.; Prokoshkin, S.; Brailovski, V. Optimization of a Thermomechanical Treatment of Superelastic Ti-Zr-Nb Alloys for the Production of Bar Stock for Orthopedic Implants. *J. Alloys Compd.* **2022**, *928*, 167143. [[CrossRef](#)]
25. Sheremetyev, V.; Dubinskiy, S.; Kudryashova, A.; Prokoshkin, S.; Brailovski, V. In Situ XRD Study of Stress- and Cooling-Induced Martensitic Transformations in Ultrafine- and Nano-Grained Superelastic Ti-18Zr-14Nb Alloy. *J. Alloys Compd.* **2022**, *902*, 163704. [[CrossRef](#)]
26. Kanapaakala, G.; Subramani, V. A Review on β -Ti Alloys for Biomedical Applications: The Influence of Alloy Composition and Thermomechanical Processing on Mechanical Properties, Phase Composition, and Microstructure. *Proc. Inst. Mech. Eng. Part L J. Mater. Des. Appl.* **2023**, *237*, 1251–1294. [[CrossRef](#)]
27. Hao, Y.L.; Yang, R.; Niinomi, M.; Kuroda, D.; Zhou, Y.L.; Fukunaga, K.; Suzuki, A. Aging Response of the Young's Modulus and Mechanical Properties of Ti-29Nb-13Ta-4.6Zr for Biomedical Applications. *Metall. Mater. Trans. A* **2003**, *34*, 1007–1012. [[CrossRef](#)]
28. Kim, H.Y.; Kim, J.I.; Inamura, T.; Hosoda, H.; Miyazaki, S. Effect of Thermo-Mechanical Treatment on Mechanical Properties and Shape Memory Behavior of Ti-(26–28) at.% Nb Alloys. *Mater. Sci. Eng. A* **2006**, *438–440*, 839–843. [[CrossRef](#)]
29. Sheremetyev, V.; Brailovski, V.; Prokoshkin, S.; Inaekyan, K.; Dubinskiy, S. Functional Fatigue Behavior of Superelastic Beta Ti-22Nb-6Zr(At%) Alloy for Load-Bearing Biomedical Applications. *Mater. Sci. Eng. C* **2016**, *58*, 935–944. [[CrossRef](#)] [[PubMed](#)]

30. Gao, J.J.; Thibon, I.; Castany, P.; Gloriant, T. Effect of Grain Size on the Recovery Strain in a New Ti–20Zr–12Nb–2Sn Superelastic Alloy. *Mater. Sci. Eng. A* **2020**, *793*, 139878. [[CrossRef](#)]
31. Zhou, Y.; Fillon, A.; Laillé, D.; Gloriant, T. Probing Grain Size Effect in the Superelastic Ti-20Zr-3Mo-3Sn Alloy Using Spherical Nanoindentation. *Mater. Charact.* **2022**, *184*, 111691. [[CrossRef](#)]
32. Inamura, T.; Shimizu, R.; Kim, H.Y.; Miyazaki, S.; Hosoda, H. Optimum Rolling Ratio for Obtaining {001}<110> Recrystallization Texture in Ti–Nb–Al Biomedical Shape Memory Alloy. *Mater. Sci. Eng. C* **2016**, *61*, 499–505. [[CrossRef](#)]
33. Jabir, H.; Fillon, A.; Castany, P.; Gloriant, T. Crystallographic Orientation Dependence of Mechanical Properties in the Superelastic Ti-24Nb-4Zr-8Sn Alloy. *Phys. Rev. Mater.* **2019**, *3*, 63608. [[CrossRef](#)]
34. Elmay, W.; Prima, F.; Gloriant, T.; Bolle, B.; Zhong, Y.; Patoor, E.; Laheurte, P. Effects of Thermomechanical Process on the Microstructure and Mechanical Properties of a Fully Martensitic Titanium-Based Biomedical Alloy. *J. Mech. Behav. Biomed. Mater.* **2013**, *18*, 47–56. [[CrossRef](#)] [[PubMed](#)]
35. Zhang, D.C.; Tan, C.G.; Tang, D.M.; Zhang, Y.; Lin, J.G.; Wen, C.E. Effect of Thermomechanical Treatment on the Superelasticity of Ti–7.5 Nb–4Mo–2Sn Biomedical Alloy. *Mater. Sci. Eng. C* **2014**, *44*, 76–86. [[CrossRef](#)] [[PubMed](#)]
36. Dubinskiy, S.; Prokoshkin, S.; Sheremetyev, V.; Konopatsky, A.S.; Korotitskiy, A.V.; Tabachkova, N.Y.; Blinova, E.N.; Glezer, A.M.; Brailovski, V. The Mechanisms of Stress-Induced Transformation in Ultimately Fine-Grained Titanium Nickelide, and Critical Grain Size for This Transformation. *J. Alloys Compd.* **2021**, 157733. [[CrossRef](#)]
37. Hanada, S.; Ozeki, M.; Izumi, O. Deformation Characteristics in β Phase Ti-Nb Alloys. *Metall. Trans. A* **1985**, *16*, 789–795. [[CrossRef](#)]
38. Lai, M.J.; Tasan, C.C.; Raabe, D. On the Mechanism of {332} Twinning in Metastable β Titanium Alloys. *Acta Mater.* **2016**, *111*, 173–186. [[CrossRef](#)]
39. Bertrand, E.; Castany, P.; Yang, Y.; Menou, E.; Gloriant, T. Deformation Twinning in the Full- α'' martensitic Ti–25Ta–20Nb Shape Memory Alloy. *Acta Mater.* **2016**, *105*, 94–103. [[CrossRef](#)]
40. Dan, A.; Cojocaru, E.M.; Raducanu, D.; Nocivin, A.; Cinca, I.; Cojocaru, V.D. {332}<113> and {112}<111> Twin Variant Activation during Cold-Rolling of a Ti-Nb-Zr-Ta-Sn-Fe Alloy. *Materials* **2022**, *15*, 6932. [[CrossRef](#)]
41. Lukashevich, K.; Sheremetyev, V.; Komissarov, A.; Cheverikin, V.; Andreev, V.; Prokoshkin, S.; Brailovski, V. Effect of Cooling and Annealing Conditions on the Microstructure, Mechanical and Superelastic Behavior of a Rotary Forged Ti–18Zr–15Nb (at.%) Bar Stock for Spinal Implants. *J. Funct. Biomater.* **2022**, *13*, 259. [[CrossRef](#)]
42. Tobe, H.; Kim, H.Y.; Miyazaki, S. Effect of Nb Content on Deformation Textures and Mechanical Properties of Ti-18Zr-Nb Biomedical Alloys. *Mater. Trans.* **2009**, *50*, 2721–2725. [[CrossRef](#)]
43. Kim, H.Y.; Miyazaki, S. Several Issues in the Development of Ti–Nb-Based Shape Memory Alloys. *Shape Mem. Superelasticity* **2016**, *2*, 380–390. [[CrossRef](#)]
44. Fu, J.; Yamamoto, A.; Kim, H.Y.; Hosoda, H.; Miyazaki, S.T. Novel Ti-Base Superelastic Alloys with Large Recovery Strain and Excellent Biocompatibility. *Acta Biomater.* **2015**, *17*, 56–67. [[CrossRef](#)] [[PubMed](#)]
45. Fu, J.; Kim, H.Y.; Miyazaki, S. Effect of Annealing Temperature on Microstructure and Superelastic Properties of a Ti-18Zr-4.5 Nb-3Sn-2Mo Alloy. *J. Mech. Behav. Biomed. Mater.* **2017**, *65*, 716–723. [[CrossRef](#)] [[PubMed](#)]
46. Prokoshkin, S.; Korotitskiy, A.V.; Brailovski, V.; Inaekyan, K.; Dubinskiy, S. Crystal Lattice of Martensite and the Reserve of Recoverable Strain of Thermally and Thermomechanically Treated Ti-Ni Shape-Memory Alloys. *Phys. Met. Metallogr.* **2011**, *112*, 170–187. [[CrossRef](#)]

Disclaimer/Publisher’s Note: The statements, opinions and data contained in all publications are solely those of the individual author(s) and contributor(s) and not of MDPI and/or the editor(s). MDPI and/or the editor(s) disclaim responsibility for any injury to people or property resulting from any ideas, methods, instructions or products referred to in the content.